



HAL
open science

Multiscale model of global inner-core anisotropy induced by hcp-alloy plasticity

A Lincot, Ph Cardin, R Deguen, Sébastien Merkel

► **To cite this version:**

A Lincot, Ph Cardin, R Deguen, Sébastien Merkel. Multiscale model of global inner-core anisotropy induced by hcp-alloy plasticity. 2016. hal-01259186v1

HAL Id: hal-01259186

<https://hal.science/hal-01259186v1>

Preprint submitted on 20 Jan 2016 (v1), last revised 21 Jan 2016 (v2)

HAL is a multi-disciplinary open access archive for the deposit and dissemination of scientific research documents, whether they are published or not. The documents may come from teaching and research institutions in France or abroad, or from public or private research centers.

L'archive ouverte pluridisciplinaire **HAL**, est destinée au dépôt et à la diffusion de documents scientifiques de niveau recherche, publiés ou non, émanant des établissements d'enseignement et de recherche français ou étrangers, des laboratoires publics ou privés.

1 Multiscale model of global inner-core anisotropy 2 induced by hcp-alloy plasticity

A. Lincot^{1,2}, Ph. Cardin¹, R. Deguen³, S. Merkel^{2,4}

3 **Key points** (100 characters max. for each)

- 4 • Multiscale model of inner-core anisotropy produced by hcp alloy deformation
- 5 • 5 to 20% single-crystal elastic anisotropy and plastic deformation by pyramidal slip
- 6 • Low-degree inner-core formation model with faster crystallization at the equator

¹Université Grenoble Alpes, CNRS,
ISTerre, F-38041 Grenoble, France.

²UMET, Unité Matériaux et
Transformations, CNRS, INRA, ENSCL,
Université de Lille, F-59000 Lille, France.

³Laboratoire de géologie de Lyon, ENS de
Lyon, Université Lyon-1, F-69007 Lyon,
France.

⁴Institut Universitaire de France, F-75005
Paris, France

7 The Earth's solid inner-core exhibits a global seismic anisotropy of sev-
8 eral percents. It results from a coherent alignment of anisotropic Fe-alloy
9 crystals through the inner-core history that can be sampled by present-
10 day seismic observations. By combining self-consistent polycrystal plastic-
11 ity, inner-core formation models, Monte-Carlo search for elastic moduli,
12 and simulations of seismic measurements, we introduce a multiscale model
13 that can reproduce a global seismic anisotropy of several percents aligned
14 with the Earth's rotation axis. Conditions for a successful model are an
15 hexagonal-close-packed structure for the inner-core Fe-alloy, plastic defor-
16 mation by pyramidal $\langle c + a \rangle$ slip, and large-scale flow induced by a low-
17 degree inner-core formation model. For global anisotropies ranging between
18 1 and 3%, the elastic anisotropy in the single crystal ranges from 5 to 20%
19 with larger velocities along the c -axis.

1. Introduction

20 Seismic observations using body waves differential travel times [*Poupinet et al.*, 1983;
21 *Morelli et al.*, 1986; *Waszek et al.*, 2011], long period normal modes [*Woodhouse et al.*,
22 1986; *Deuss et al.*, 2010], and the analysis of autocorrelation of earthquake coda [*Wang*
23 *et al.*, 2015] provide strong evidences that the Earth's inner-core is anisotropic, with *P*-
24 waves traveling faster by up to 3% in the polar than in the equatorial direction. Further
25 analyses refined this observation, providing evidences for both hemispherical and radial
26 variations of the amplitude of anisotropy [*Tkalčić*, 2015; *Deuss*, 2014; *Wang et al.*, 2015].
27 However, this apparent complexity should not obscure the first-order observation that the
28 fast propagation direction for inner-core seismic waves is aligned with the Earth's rotation
29 axis. The observed axial anisotropy still lacks a conclusive explanation. This paper will
30 hence focus on reproducing this first-order observation from a multiscale model.

31 A multiscale model of inner-core anisotropy should allow to build a synthetic inner-core
32 with a given choice of crystal structure, elastic moduli, and crystal alignment mechanism,
33 coupled with an inner-core formation hypothesis. In a second stage, the model should
34 simulate present-day seismic observations which can then be compared with actual mea-
35 surements [Fig. 1, *Lincot et al.*, 2014].

36 In this work, we investigate whether such integrated model can indeed reproduce the
37 first-order observation of several percents North-South global seismic anisotropy in the
38 inner-core. The abundance of symmetries for elasticity and plasticity of body-centered-
39 cubic (bcc) and face-centered-cubic (fcc) phases combined with the integrated nature
40 of inner-core anisotropy measurements is such that plastic deformation of such crystal

41 structures cannot explain the global inner-core anisotropy [*Lincot et al.*, 2015]. Here, we
42 investigate the effect of an hexagonal-close-packed (hcp) structure for the inner-core Fe
43 alloy. Under the assumption that the inner-core anisotropy results from plastic defor-
44 mation along a dominant slip system, we find that necessary conditions for a successful
45 anisotropic model are 5 to 20% single crystal elastic anisotropy, plastic deformation by
46 pyramidal slip, and a large-scale flow induced by a low-degree inner-core formation model.

2. Methods

2.1. Inner-core formation model

47 It is typically assumed that the inner-core anisotropic structure results from an align-
48 ment of anisotropic Fe-alloy crystals acquired either during solidification [*Bergman*, 1997;
49 *Deuss et al.*, 2010] or as a result of subsequent deformation [*Yoshida et al.*, 1996; *Karato*,
50 1999; *Wenk et al.*, 2000a; *Deguen*, 2012] although other models have been proposed as-
51 suming, for instance, the presence of aligned aspherical liquid inclusions in the inner-core
52 [*Singh et al.*, 2000].

53 Radial dendritic growth [*Bergman*, 1997] aligns the crystals relative to the spherical
54 inner-core boundary (ICB) which is unlikely to produce a global cylindrical axisymmetric
55 anisotropy [*Lincot et al.*, 2014]. An additional orientation mechanism is required for
56 aligning the fast P -wave crystal directions with the Earth's rotation axis. Two classes
57 of processes have been suggested in the literature: (i) a forcing of inner-core dynamics
58 from the outer core magnetic field [*Karato*, 1999; *Buffett and Wenk*, 2001] (ii) an effect
59 of the Earth's rotation through the ellipticity of a convective inner-core [*Buffett*, 2009] or
60 inner-core preferential growth [*Yoshida et al.*, 1996]. Recent studies evaluated that the

61 direct effect of the Lorentz forcing generates weak deformation [Lasbleis *et al.*, 2015]. The
 62 effect of the magnetic field on anisotropy would result from solidification textures mostly,
 63 which are not well understood at inner-core conditions and have not been observed in
 64 analogue experiments [Brito *et al.*, 2002]. In addition, recent calculations of the thermal
 65 conductivity of Fe at core conditions [Zhang *et al.*, 2015] indicate that thermal convection
 66 is unlikely in the inner-core [Deguen, 2012], although compositional convection may be
 67 an option [Gubbins *et al.*, 2013].

68 We therefore focus on models of inner-core growth with faster solidification in the equa-
 69 torial plane [Fig. 2a, Yoshida *et al.*, 1996], with solidification texturing [Fig. 2b, Bergman,
 70 1997] and/or density stratification [Fig. 2c, Deguen and Cardin, 2009] as possible addi-
 71 tional ingredients. In all cases, we impose a solidification rate twice as large at the equator
 72 than at the poles. Model *a)* assumes random solidification textures while model *b)* in-
 73 cludes solidification textures in which the *c*-axes of the hcp crystals lie preferentially in
 74 the plane of the ICB. Model *c)* accounts for a stable density stratification during inner-
 75 core formation. The importance of stratification depends on the value of the buoyancy
 76 number $\mathcal{B}^* = \frac{\Delta\rho g r_{ic}^2}{\eta \dot{r}_{ic}}$, where $\Delta\rho$ is the density difference across the inner core associated
 77 with compositional or thermal stratification (excluding the contribution of compression),
 78 g the acceleration of gravity at the ICB, η the dynamic viscosity of the inner core, r_{ic} the
 79 inner core radius and \dot{r}_{ic} the inner core growth rate [Deguen and Cardin, 2009]. Density
 80 stratification tends to localize the deformation in a thin shear layer below the ICB, whose
 81 thickness decreases with increasing $|\mathcal{B}|$, and in which the strain rate increases with $|\mathcal{B}|$.
 82 In this study, we set $\mathcal{B}^* = -10^6$ (corresponding to $\Delta\rho \simeq 5 \text{ kg.m}^{-3}$ and $\eta \simeq 10^{18} \text{ Pa.s}$).

83 Larger \mathcal{B}^* values would result in earlier stratification in the Earth's history and and, con-
84 sequently, reduce the central part of pure shear deformation [*Deguen and Cardin, 2009;*
85 *Deguen et al., 2011*]. Also note that model *c*) assumes random solidification textures at
86 the ICB. Deformation is large in such model and, hence, solidification textures are quickly
87 erased and do not play an important role in the modeled global scale anisotropy, as in
88 this study, but can play a crucial role for studies focused on the superficial layer of the
89 inner-core.

90 As illustrated in Fig. 2, a model reproducing present day seismic observations should
91 integrate the whole history of the inner-core. In that view, seismic anisotropy is a marker
92 of inner-core formation and evolution and will record changes in dynamics or mineralogy
93 during its history.

2.2. Inner-core Fe-alloy textures

94 For each inner-core formation model, we assume plastic deformation of the inner-core
95 Fe-alloy on a dominant slip system. We follow the deformation of 100 markers introduced
96 at the ICB during inner-core growth and calculate the corresponding textures for a 10000
97 grains aggregate using the visco-plastic self-consistent (VPSC) code of *Lebensohn and*
98 *Tomé* [1993]. Experiments on Fe and analogues indicate that basal slip and twinning
99 dominate the plastic behavior of hcp-Fe at low temperature [*Wenk et al., 2000b; Merkel*
100 *et al., 2004*] and that, as temperature increases, twinning disappears and the activity
101 of pyramidal $\langle c + a \rangle$ slip increases [*Poirier and Langenhorst, 2002; Miyagi et al., 2008;*
102 *Merkel et al., 2012*]. We simulate the texture of an hcp aggregate at each marker for three

103 different dominant slip systems: basal, prismatic and pyramidal $\langle c + a \rangle$ (Table 1). The
 104 final results are meridional maps of textures for a present day inner-core (Fig. 3).

105 This results in a striking observation: simulations with the pyramidal $\langle c + a \rangle$ slip system
 106 are very efficient at aligning the c -axes of the polycrystals with the Earth's rotation axis.
 107 Simulations with other slip systems can induce strong textures at the local scale but, over
 108 the scale of the inner core, the hcp-alloy alignment is not consistent. Indeed, unlike basal
 109 and prismatic slip, pyramidal $\langle c + a \rangle$ slip includes c in the slip direction: it is prone to
 110 align the c -axes of the aggregate during deformation.

2.3. Inner-core elasticity

111 Given the spread of published data for the elasticity of hcp-Fe at inner-core conditions
 112 [Vočadlo *et al.*, 2009; Sha and Cohen, 2010; Martorell *et al.*, 2013] and the unknown
 113 influence of alloying elements, we estimate the global inner-core anisotropy as a function
 114 of single-crystal elasticity over a wide range of values. Rather than using grid points in
 115 the five-dimensional space of independent elastic constants, we generate elastic moduli by
 116 a Monte-Carlo approach.

117 We generate 4500 random sets of single-crystal elastic moduli which satisfy the following
 118 requirements. The Hill average of the bulk and shear moduli of the randomly oriented
 119 aggregate should be within 15% of inner-core values [$K = 1400$ GPa and $G = 170$ GPa,
 120 *Dziewoński and Anderson*, 1981]. The single-crystal elastic moduli should also satisfy
 121 conditions for mechanical stability for hcp [*Wallace*, 1972]

$$C_{11} - C_{12} > 0; \tag{1}$$

$$C_{11} + C_{12} + C_{33} > 0;$$

$$(C_{11} + C_{12})C_{33} - 2 C_{13}^2 > 0;$$

$$C_{44} > 0,$$

122 where C_{ij} are single-crystal elastic moduli.

123 For each inner-core formation model, elastic model, and marker position, we calculate
 124 the polycrystalline elastic tensor using the simulated textures and single-crystal elastic
 125 moduli.

2.4. Inner-core seismic anisotropy

126 More than 300000 synthetic seismic rays are generated randomly to probe the whole
 127 inner-core. For each ray, we estimate the normalized seismic travel times residual $\delta t/t =$
 128 $(s - s^0)/s^0$ where s is the simulated slowness of the seismic ray, and s^0 is the slowness of
 129 that same ray for an homogeneous and fully isotropic inner-core [*Lincot et al.*, 2014].

Many seismological studies use averaging procedures with travel times residuals fitted
 to [*Creager*, 1992; *Deuss*, 2014]

$$\delta t/t = a_1 + a_2 \cos^2 \zeta + a_3 \cos^4 \zeta, \quad (2)$$

130 where a_1 , a_2 and a_3 are adjustable parameters and ζ is the angle between the ray and the
 131 Earth rotation axis. The quantity $a_2 + a_3$ is the difference between polar ($\zeta = 0^\circ$) and
 132 equatorial ($\zeta = 90^\circ$) residuals. It is a measure of the global inner-core anisotropy often
 133 reported in the literature. It will be used in the rest of the paper (Fig. 4).

3. Results

3.1. Parameters for hcp single-crystal anisotropy

134 Despite the complexity introduced by elasticity, crystal plasticity, geodynamics, and
 135 seismic rays geometry, two dimensionless elastic parameters are found to primarily affect
 136 the global inner-core anisotropy: Δ^{c-a} and Δ^{45° . Δ^{c-a} describes the relative difference
 137 in P -waves velocities along the c - and a -axes (V_P^c and V_P^a), and Δ^{45° is related to the
 138 concavity of the single-crystal P -wave velocities, 45° away from the c -axis ($V_P^{45^\circ}$). They
 139 are calculated as follow

$$\begin{aligned}\Delta^{c-a} &= \frac{V_P^c - V_P^a}{V_P^m}, \\ \Delta^{45^\circ} &= \frac{V_P^{45^\circ} - (V_P^c + V_P^a)/2}{V_P^m},\end{aligned}\tag{3}$$

140 where V_P^m is the average P -wave velocity.

141 Global anisotropy results are consistent when plotted as a function of Δ^{c-a} and Δ^{45° :
 142 they reveal parallel isocontour mainly controlled by Δ^{c-a} (Fig. 4). This analysis allows to
 143 classify our 4500 sets of random elastic moduli and other calculations from the literature
 144 in a simple representation and estimate their effect on global inner-core anisotropy.

3.2. Inner-core anisotropy

145 Seismic studies report global inner core anisotropy of up to several percents with North-
 146 South velocities larger than those in the equatorial plane [Deuss, 2014; Tkalčić, 2015]. As
 147 shown in Fig. 4, this level of anisotropy is difficult to reach if deformation of the inner-core
 148 hcp-alloy is controlled by dominant basal or prismatic slip, irrespectively of the inner-core
 149 formation model. Indeed, inner-core anisotropy is measured with waves crossing the entire

150 inner core. If polycrystalline textures are not consistent over large regions, the anisotropy
151 of the single-crystal will be canceled at the global scale of the seismic measurement.

152 Pyramidal $\langle c + a \rangle$ slip, on the other hand, is prone to align the c -axes of an aggregate
153 during its deformation. Hexagonal crystals are axisymmetric around the single-crystal
154 c -axis for elasticity. As such, this mechanism allows for significant enhancement of the
155 global scale inner-core anisotropy. With dominant pyramidal $\langle c + a \rangle$ slip, faster velocities
156 along single-crystal c -axes ($\Delta^{c-a} > 0$) are required to obtain a positive global anisotropy.
157 Δ^{45° acts as a secondary but non negligible factor: a concave variation of the velocities
158 ($\Delta^{45^\circ} > 0$) tends to amplify the global anisotropy.

159 Models with dominant pyramidal $\langle c + a \rangle$ slip, faster crystallization in the equatorial
160 region, and random crystallization textures at the solidification front produce global
161 anisotropies 5 to 15 times smaller than Δ^{c-a} at the single-crystal level. The addition
162 of solidification textures enhances the global anisotropy but also adds scatter in the rep-
163 resentation of Fig. 4 with a few models with $\Delta^{c-a} < 10\%$ producing a global anisotropy
164 larger than 3%. In such model, textures produced in the central portions of the inner-core
165 are induced by plastic deformation, with a global cylindrical symmetry, whereas the outer
166 portions of the inner-core are mostly influenced by solidification textures with a global
167 spherical symmetry (Fig. 3). This induces heterogeneities in travel time calculations and
168 scatter in the representation of Fig. 4. The addition of stratification reinforces the global
169 anisotropy by up to 50%. For example, in the stratified model with dominant pyramidal
170 $\langle c + a \rangle$ slip, single-crystal anisotropies with Δ^{c-a} between 5 and 20% are required for a
171 global anisotropy between 1 and 3%.

4. Discussion and conclusion

172 Previous studies have shown that bcc and fcc phases orientation through dislocation
 173 creep cannot explain the observed North-South global inner-core anisotropy [*Lincot et al.*,
 174 2015] . Here, we show that an hcp inner-core Fe-alloy, deforming plastically along a dom-
 175 inant pyramidal $\langle c + a \rangle$ slip system, with 5 to 20% elastic anisotropy in the single-crystal,
 176 and a simple low-degree inner-core formation model can produce a global anisotropy of 1
 177 to 3%.

178 Hexagonal crystals are axisymmetric around their c -axis for elasticity. As such, a most
 179 efficient model of inner-core anisotropy should align the c -axes of the hcp aggregates with
 180 the Earth's rotation axis. This ingredient is crucial for reproducing inner-core anisotropy
 181 and can be obtained if the plasticity of the inner-core hcp-alloy is dominated by pyramidal
 182 $\langle c + a \rangle$ slip.

183 Fig. 4 allows for constraining Δ^{c-a} and Δ^{45° for single-crystal elastic tensors compat-
 184 ible with anisotropy observations. Do note, however, that our solution for single-crystal
 185 elasticity is not unique. First-principles calculations for stable hcp-Fe at inner-core condi-
 186 tions [*Vočadlo et al.*, 2009; *Sha and Cohen*, 2010] lead to a weak single-crystal anisotropy
 187 and weak global anisotropy, below 1% (Fig. 4). Recently, it was shown that hcp-Fe may
 188 exhibit a strong nonlinear shear weakening just before melting, with a reduction in V_S
 189 and a large increase in single-crystal anisotropy [*Martorell et al.*, 2013]. With such elas-
 190 tic moduli, our multi-scale model is successful at reproducing inner-core global seismic
 191 anisotropy (Fig. 4).

192 A large-scale coherent alignment of anisotropic Fe-alloy through the inner-core is re-
193 quired to reproduce a North-South global seismic anisotropy, which likely requires that
194 crystal alignment is due to a low-degree deformation field. A more complex geometry like,
195 for example, high Rayleigh number convection, could generate locally strong textures but
196 such anisotropy would be canceled at the scale of seismic observations.

197 At this point, other details of the scenario of inner-core formation can not be discrimi-
198 nated. Observations of inner-core anisotropy are constrained by a distinct set of specific
199 ray paths – a few hundreds – that are now being supplemented by the addition of vir-
200 tual paths using the cross-correlation of ambient noise and earthquake coda [*Wang et al.*,
201 2015; *Boué et al.*, 2014]. In addition, the representation of seismic observations with fits
202 (Eq. 2) oversimplifies the data by smoothing the geographical and depth dependence of
203 the seismic travel times. In the future, such direct multi-scale model should be extended
204 for inverting the actual observations of seismic travel times, including their radial and
205 lateral variations [*Deuss*, 2014; *Tkalčić*, 2015; *Wang et al.*, 2015]. This new approach will
206 constrain the different scenarios regarding the history of the Earth’s inner-core and its
207 interactions with the outer core [*Deguen*, 2012] and the geodynamo [*Aubert et al.*, 2008].

208 **Acknowledgments.** The authors wish to thank Mathieu Dumberry, the Geodynamo
209 group at ISTerre, and the Mineral Physics group at UMET for useful discussions as well as
210 Mike Bergman and Shigeo Yoshida for constructive reviews. This work has been financed
211 by the program PNP of CNRS/INSU and labex OSUG@2020. RD acknowledges support
212 from grant ANR-12-PDOC-0015-01 of the ANR (Agence Nationale de la Recherche).

213 Calculations were made at Centre de Calcul Commun of the OSUG. Data used in this
214 paper are available upon request.

References

- 215 Aubert, J., H. Amit, G. Hulot, and P. Olson, Thermochemical flows couple the
216 Earth's inner core growth to mantle heterogeneity, *Nature*, *454*, 758–761, doi:
217 10.1038/nature07109, 2008.
- 218 Bergman, M. I., Measurements of elastic anisotropy due to solidification texturing and
219 the implication for the Earth's inner core, *Nature*, *389*, 60–63, doi:10.1038/37962, 1997.
- 220 Boué, P., P. Poli, M. Campillo, and P. Roux, Reverberations, coda waves and ambient
221 noise: Correlations at the global scale and retrieval of the deep phases, *Earth and*
222 *Planetary Science Letters*, *391*, 137–145, 2014.
- 223 Brito, D., D. Elbert, and P. Olson, Experimental crystallization of gallium: Ultrasonic
224 measurements of elastic anisotropy and implications for the inner core, *Phys. Earth*
225 *Planet. Int.*, *129*, 325–346, doi:10.1016/S0031-9201(01)00298-9, 2002.
- 226 Buffett, B. A., Onset and orientation of convection in the inner core, *Geophys. J. Int.*,
227 *179*, 711–719, doi:10.1111/j.1365-246X.2009.04311.x, 2009.
- 228 Buffett, B. A., and H.-R. Wenk, Texturing of the Earth's inner core by Maxwell stresses,
229 *Nature*, *413*, 60–63, doi:10.1038/35092543, 2001.
- 230 Creager, K. C., Anisotropy of the inner core from differential travel times of the phases
231 PKP and PKIKP, *Nature*, *356*, 309–314, doi:10.1038/356309a0, 1992.
- 232 Deguen, R., Structure and dynamics of Earth's inner core, *Earth Planet. Sci. Lett.*, *333-*
233 *334*, 211–225, doi:10.1016/j.epsl.2012.04.038, 2012.

- 234 Deguen, R., and P. Cardin, Tectonic history of the Earth's inner core preserved in its
235 seismic structure, *Nature Geoscience*, *2*, 419 – 422, doi:10.1038/ngeo522, 2009.
- 236 Deguen, R., S. Merkel, R. A. Lebensohn, and P. Cardin, Texturing in Earths inner core
237 due to preferential growth in its equatorial belt, *Phys. Earth Planet. Inter.*, *188*, 173–
238 184, doi:10.1016/j.pepi.2011.08.008, 2011.
- 239 Deuss, A., Heterogeneity and anisotropy of Earth's inner core, *Ann. Rev. Earth Planet.*
240 *Sc.*, *42*, 103–126, doi:10.1146/annurev-earth-060313-054658, 2014.
- 241 Deuss, A., J. C. E. Irving, and J. H. Woodhouse, Regional variation of inner core
242 anisotropy from seismic normal mode observations, *Science*, *328*(5981), 1018–1020, doi:
243 10.1126/science.1188596, 2010.
- 244 Dziewoński, A. M., and D. L. Anderson, Preliminary reference Earth model, *Phys. Earth*
245 *Planet. Inter.*, *25*, 297–356, 1981.
- 246 Gubbins, D., D. Alfè, and C. J. Davies, Compositional instability of earth's solid inner
247 core, *Geophys Res. Lett.*, *40*, 10841088, doi:10.1002/grl.50186, 2013.
- 248 Karato, S., Seismic anisotropy of the Earth's inner core resulting from flow induced
249 Maxwell stresses, *Nature*, *402*, 871–873, doi:10.1038/47235, 1999.
- 250 Lasbleis, M., R. Deguen, P. Cardin, and S. Labrosse, Earths inner core dynamics induced
251 by the Lorentz force, *Geophys. J. Int.*, *202*, 548–563, doi:10.1093/gji/ggv155, 2015.
- 252 Lebensohn, R. A., and C. N. Tomé, A selfconsistent anisotropic approach for the simu-
253 lation of plastic deformation and texture development of polycrystals: application to
254 zirconium alloys, *Acta Metall. Mater.*, *41*, 2611–2624, 1993.

- 255 Lincot, A., R. Deguen, S. Merkel, and P. Cardin, Seismic response and anisotropy of a
256 model hcp iron inner core, *C R Geosci*, *346*, 148–157, doi:10.1016/j.crte.2014.04.001,
257 2014.
- 258 Lincot, A., S. Merkel, and P. Cardin, Is inner core seismic anisotropy a marker of plastic
259 flow of cubic iron?, *Geophys Res. Lett.*, *42*, 13261333, doi:10.1002/2014GL062862, 2015.
- 260 Martorell, B., L. Vočadlo, J. Brodholt, and I. G. Wood, Strong premelting effect in the
261 elastic properties of hcp-fe under inner-core conditions, *Science*, *342*, 466–468, doi:
262 10.1126/science.1243651, 2013.
- 263 Merkel, S., H.-R. Wenk, P. Gillet, H. K. Mao, and R. J. Hemley, Deformation of poly-
264 crystalline iron up to 30 GPa and 1000 K, *Phys. Earth Planet. Inter.*, *145*, 239–251,
265 2004.
- 266 Merkel, S., M. Gruson, Y. Wang, N. Nishiyama, and C. N. Tomé, Texture and elas-
267 tic strains in hcp-iron plastically deformed up to 17.5 GPa and 600 K: experi-
268 ment and model, *Modelling Simul. Mater. Sci. Eng.*, *20*, 024,005, doi:10.1088/0965-
269 0393/20/2/024005, 2012.
- 270 Miyagi, L., M. Kunz, J. Knight, J. Nasiatka, M. Voltolini, and H.-R. Wenk, In situ phase
271 transformation and deformation of iron at high pressure and temperature, *J. Appl.*
272 *Phys.*, *104*, 103,510, doi:10.1063/1.3008035, 2008.
- 273 Morelli, A., A. M. Dziewoński, and J. H. Woodhouse, Anisotropy of the inner core inferred
274 from PKIKP travel times, *Geophys. Res. Lett.*, *13*, 1545–1548, 1986.
- 275 Poirier, J. P., and F. Langenhorst, TEM study of an analogue of the Earth’s inner core ϵ -
276 Fe, *Phys. Earth Planet. Inter.*, *129*, 347–358, doi:10.1016/S0031-9201(01)00300-4, 2002.

- 277 Poupinet, G., R. Pillet, and A. Souriau, Possible heterogeneity of the Earth's inner core
278 deduced from PKIKP travel times, *Nature*, *305*, 204–206, doi:10.1038/305204a0, 1983.
- 279 Sha, X., and R. E. Cohen, Elastic isotropy of ϵ -Fe under Earth's core conditions, *Geophys.*
280 *Res. Lett.*, *37*, L10,302, doi:10.1029/2009GL042224, 2010.
- 281 Singh, S. C., M. A. J. Taylor, and J. P. Montagner, On the presence of liquid in the
282 Earth's inner core, *Science*, *287*, 2471–2474, 2000.
- 283 Tkalčić, H., Complex inner core of the Earth: The last frontier of global seismology, *Rev.*
284 *Geophys.*, *53*, doi:10.1002/2014RG000469, 2015.
- 285 Vočadlo, L., D. P. Dobson, and I. G. Wood, Ab initio calculations of the elasticity of
286 hcp-Fe as a function of temperature at inner-core pressure, *Earth Planet. Sci. Lett.*, *288*,
287 534–538, doi:10.1016/j.epsl.2009.10.015, 2009.
- 288 Wallace, D. C., *Thermodynamics of Crystals*, Wiley, New York, 1972.
- 289 Wang, T., X. Song, and H. H. Xia, Equatorial anisotropy in the inner part of Earth's
290 inner core from autocorrelation of earthquake coda, *Nat. Geosci.*, *8*, 224–227, doi:
291 10.1038/ngeo2354, 2015.
- 292 Waszek, L., J. Irving, and A. Deuss, Reconciling the hemispherical structure of Earth's
293 inner core with its super-rotation, *Nat. Geosci.*, *4*, 264–267, doi:10.1038/ngeo1083, 2011.
- 294 Wenk, H.-R., J. R. Bamgardner, R. A. Lebensohn, and C. N. Tomé, A convection model
295 to explain the anisotropy of the inner core, *J. Geophys. Res.*, *105*, 5663–5677, 2000a.
- 296 Wenk, H.-R., S. Matthies, R. J. Hemley, H. K. Mao, and J. Shu, The plastic defor-
297 mation of iron at pressures of the Earth's inner core, *Nature*, *405*, 1044–1047, doi:
298 10.1038/35016558, 2000b.

299 Woodhouse, J. H., D. Giardini, and X. D. Li, Evidence for inner core anisotropy from free
300 oscillations, *Geophys. Res. Lett.*, *13*, 1549–1552, 1986.

301 Yoshida, S., I. Sumita, and M. Kumazawa, Growth model of the inner core coupled with
302 outer core dynamics and the resultant elastic anisotropy, *J. Geophys. Res.*, *101*, 28,085–
303 28,103, 1996.

304 Zhang, P., R. E. Cohen, and K. Haule, Effects of electron correlations on transport prop-
305 erties of iron at Earth’s core conditions, *Nature*, *517*, 605–607, doi:10.1038/nature14090,
306 2015.

Slip system		Dominant slip system			
		Basal	Prismatic	Pyr. $\langle c + a \rangle$ 1	Pyr. $\langle c + a \rangle$ 2
Basal	$(0001) \langle 11\bar{2}0 \rangle$	0.5	1.0	2.0	2.0
Prismatic	$\{1\bar{1}00\} \langle 11\bar{2}0 \rangle$	1.0	0.5	2.0	2.0
Pyr. $\langle a \rangle$	$\{1\bar{1}01\} \langle 11\bar{2}0 \rangle$	3.0	3.0	3.0	3.0
Pyr. $\langle c + a \rangle$ 1st order	$\{\bar{1}011\} \langle 11\bar{2}3 \rangle$	2.0	2.0	0.5	∞
Pyr. $\langle c + a \rangle$ 2d order	$\{\bar{1}\bar{1}22\} \langle 11\bar{2}3 \rangle$	∞	∞	∞	0.5

Table 1. Normalized critical resolved shear stresses used for calculating the development of texture in the hcp aggregate for models with the following dominant slip systems: basal, prismatic, pyramidal $\langle c + a \rangle$ first order, pyramidal $\langle c + a \rangle$ second order. The pyramidal $\langle a \rangle$ slip system is weakly activated in all cases. Results for simulations using both pyramidal $\langle c + a \rangle$ slip systems are nearly identical and are presented together in the paper.

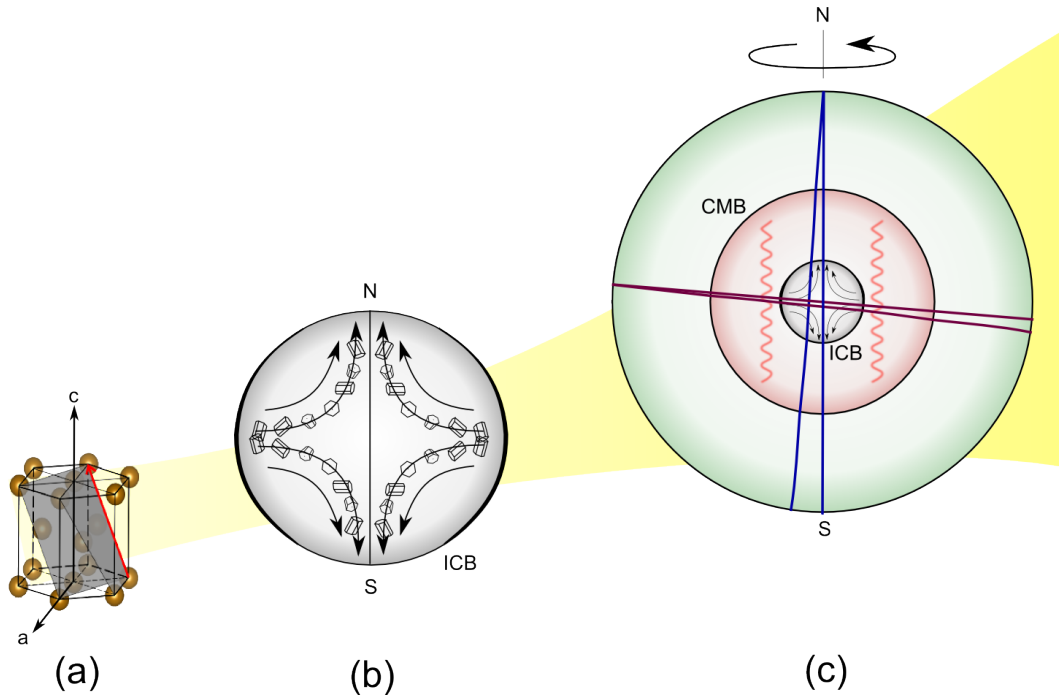


Figure 1. Multi-scale model of inner-core anisotropy. Anisotropic hexagonal Fe-alloy crystals (*a*) plastically rotate through slip under the action of deformation in the inner-core (*b*). Deformation in the inner-core depends on the core formation model, driven by heat extracted by outer core convection (*c*). At the global scale, seismic anisotropy is measured with body-wave differential travel times (*c*) which are faster along the North-South axis (blue trajectories) than in the equatorial plane (red trajectories).

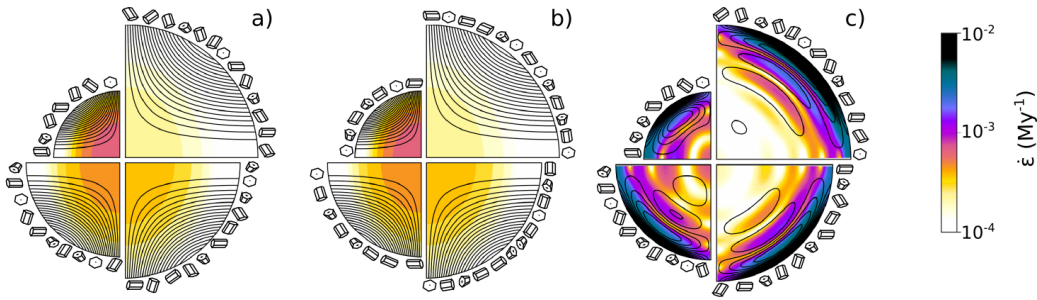


Figure 2. Inner-core formation models with preferential growth of the inner-core at the equator [Yoshida *et al.*, 1996]. The resulting topography is continuously relaxed by a quadrupolar flow, generating plastic deformation of the inner core Fe-Alloy. Model *a*) assumes random crystallization textures at the ICB while model *b*) adds solidification textures in which the *c*-axes of the hcp crystals lie preferentially in the plane of the ICB. Model *c*) accounts for a stable density stratification during inner-core formation. Each figure shows the time evolution of flow during the inner-core history at non-dimensional times $t = 0.25, 0.5, 0.75$ and 1 , where 0 is the formation of the inner-core and 1 is the present day, starting anticlockwise from the upper left quadrant. Colors are Von-mises equivalent strain rate $\dot{\epsilon}$ (in Myr^{-1} , log scale). Black lines in overlay are representative streamlines.

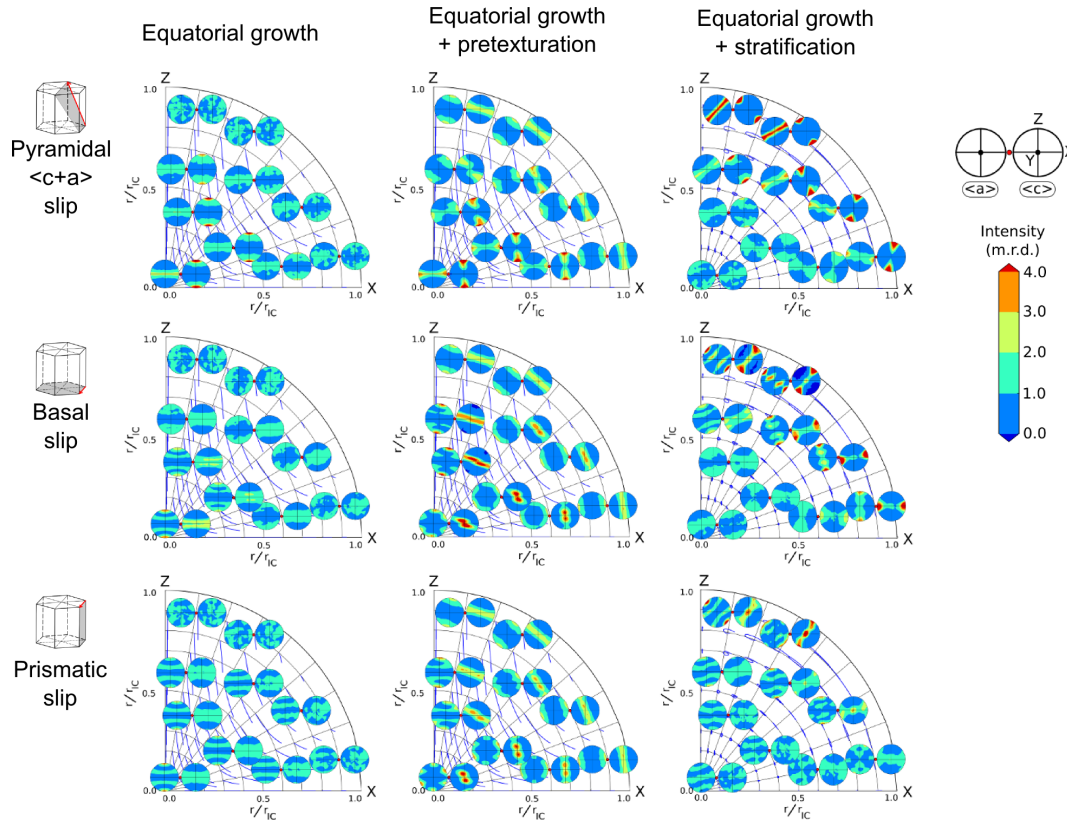


Figure 3. Pairs of pole figures of the a (left) and c (right) directions representing present-day textures of the inner-core hcp alloy. Calculated with dominant pyramidal $\langle c+a \rangle$ slip (top row), basal slip (middle row), or prismatic slip (bottom row). Core formation models with fast crystallization at the equator (left), with the addition of crystallization textures at the ICB (center), or density stratification (right). The vertical Z axis is the geographical South-North axis while X lies in the equatorial plane. Blue lines are the trajectories of the polycrystalline aggregates after crystallization at the ICB. Contours in multiples of a random distribution (m.r.d., linear scale). r_{ic} is the inner-core radius. Pyramidal slip produces the strongest global textures, with the c -axes of the aggregate mostly aligned with the Earth's rotation axis. Simulation with other slip systems produce less consistent textures, in which the c -axes of the aggregates can be found in multiple orientations.

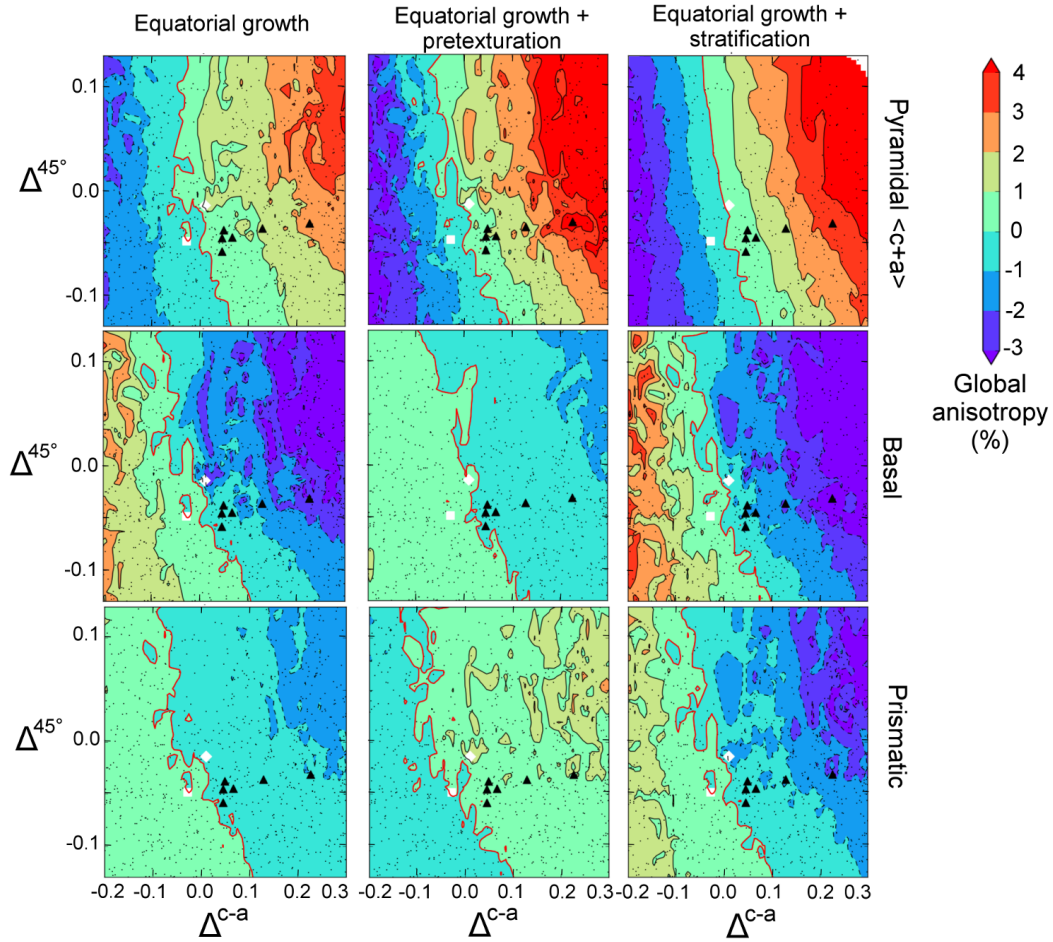


Figure 4. Global inner-core anisotropy (color scale) vs. single-crystal anisotropy parameters Δ^{c-a} and Δ^{45° for different core-formation models (columns) and dominant hcp slip systems (rows). Calculations were performed for 4500 random sets of elastic moduli (black dots) and the contour lines are obtained by interpolation. First-principles calculations for hcp-Fe single-crystal elasticity at inner-core conditions are shown as white diamond for *Vočadlo et al.* [2009], white square for *Sha and Cohen* [2010], and black triangles for *Martorell et al.* [2013] that include an effect of premelting.